

# Bifurcations and Chaos in Taylor-Green Dynamo

R. Yadav\*, M. K. Verma\*, M. Chandra\*, S. Paul\* and P. Wahi†

\*Department of Physics, Indian Institute of Technology, Kanpur, India

†Department of Mechanical Engineering, Indian Institute of Technology, Kanpur, India

**Abstract.** We present simulation results near the dynamo transition for the Taylor-Green dynamo for magnetic Prandtl number,  $P_M$ , of 0.5 and 1. We construct bifurcation diagrams for one of the dominant Fourier mode,  $\mathbf{B}(0,0,1)$ , and the ratio of magnetic and kinetic energy ( $E^b/E^u$ ) as a function of the forcing amplitude of Taylor-Green forcing. It is observed that the dynamo transition for  $P_M = 1$  is via a supercritical bifurcation, while that for  $P_M = 0.5$  is via a subcritical bifurcation. The ratio  $E^b/E^u$  varies from 0 to 3 for  $P_M = 1$ , but it is typically less than 1 for  $P_M = 0.5$ . Different dynamo states, such as those with constant, time-periodic, quasiperiodic, and chaotic magnetic fields, have been reported. We also observe coexisting dynamo states.

**Keywords:** Dynamo, Bifurcation, Magnetohydrodynamics, Direct numerical simulations

**PACS:** 91.25.Cw, 52.65.Kj, 47.20.Ky

## INTRODUCTION

Self-generation of large scale magnetic fields in astrophysical bodies (e.g., planets, stars, galaxies, and galactic clusters) is an important problem of classical physics. Larmor [1] first proposed that the swirling and twisting fluid flow can churn the remnant magnetic field in such way that the small seed magnetic field is enhanced. Later theoretical and numerical studies [2, 3] bolstered this claim. Refer to Brandenburg and Subramanian's [4] review article for the recent advances in the field.

Achieving dynamo mechanism in laboratory environment has been a long-standing goal that was accomplished only recently. Dynamo was successfully demonstrated at Riga dynamo facility in 2001 [5, 6]. Dynamo was also observed in the Karlsruhe experiment [7] in the same year. These, however, are examples of “constrained dynamo” because of their high degree of constraints on the flow. Dynamo in an unconstrained geometry was demonstrated successfully for the first time by Monchaux *et al.* [8] in 2007 in a sodium experiment known as VKS (Von Kármán Sodium). VKS team observed dynamo configurations such as constant, periodic, quasiperiodic, and chaotic magnetic fields [9, 10, 11]. The primary dynamo bifurcations observed in VKS is supercritical. Refer to Pétrélis *et al.* [12] for a more detailed discussion on experimental dynamos.

Researchers have simulated dynamo using direct numerical simulations (DNS) for various velocity configurations and geometries. Many simulations have been performed on box geometries due to relative ease of construction and reasonable computational cost. Some of the relevant and popular dynamo configurations are Taylor-Green (TG), ABC, and Roberts. TG dynamo has certain similarity with the velocity field observed in the VKS experiment. Therefore, many researchers [13, 14, 15, 16, 17] have simulated TG dynamo and have observed many interesting features, including an increase of the critical magnetic Reynolds number with the inverse of magnetic Prandtl number. Our

simulation study also focuses on TG dynamo.

Researchers [18, 19] have also attempted to understand dynamo action using low-dimensional models. DNS is concerned with taking into consideration all the accessible modes in the system (e.g.,  $64^3$  in our case), while low-dimensional models only take care of few energetic modes, and work on the assumption that the system dynamics is largely governed by these modes. Since, only a small number of equations are involved in such models, they are suitable for detailed bifurcation analysis of dynamo. However, in this study, we did not analyze the system using any low-dimensional model.

There are many unresolved issues in dynamo. Some of the current problems of interest are: what are the primary and secondary bifurcations of dynamo? How is dynamo mechanism affected by the variation of the magnetic Prandtl number? Why does the solar magnetic field show a periodic reversal behavior, while Earth's magnetic field shows random reversals? Why does the observed magnetic field have large scale structures despite turbulent nature of the fluid flow? What makes the geodynamo so efficient that its total magnetic energy is around three orders of magnitude larger than the total kinetic energy, while for the solar dynamo, the magnetic energy is smaller than total kinetic energy? etc. In the present paper we attempt to address the issues of bifurcations, and the magnetic and kinetic energies of dynamo under Taylor-Green forcing.

## EQUATIONS AND METHOD

Dynamo is observed in magnetohydrodynamics, whose equations are as follows:

$$\partial_t \mathbf{u} + (\mathbf{u} \cdot \nabla) \mathbf{u} = -\nabla p + (\mathbf{B} \cdot \nabla) \mathbf{B} + \nu \nabla^2 \mathbf{u} + \mathbf{F}, \quad (1)$$

$$\partial_t \mathbf{B} + (\mathbf{u} \cdot \nabla) \mathbf{B} = (\mathbf{B} \cdot \nabla) \mathbf{u} + \eta \nabla^2 \mathbf{B}, \quad (2)$$

$$\nabla \cdot \mathbf{u} = 0, \quad (3)$$

$$\nabla \cdot \mathbf{B} = 0, \quad (4)$$

where  $\mathbf{u}$  is the velocity,  $\mathbf{B}$  is the magnetic field,  $p$  is the total pressure (thermal+magnetic),  $\nu$  is the kinematic viscosity,  $\eta$  is the magnetic diffusivity, and  $\mathbf{F}$  is the external forcing. The velocity field is time-advanced using the Navier-Stokes equation [Eq. (1)], while the induction equation [Eq. (2)] advances the magnetic field. Eqs. (3,4) are the divergence-free conditions for the velocity field and the magnetic field, respectively.

We choose Taylor-Green (TG) forcing to excite the dynamo. TG forcing is defined as

$$\mathbf{F}(k_0) = F_0 \begin{bmatrix} \sin(k_0 x) \cos(k_0 y) \cos(k_0 z) \\ -\cos(k_0 x) \sin(k_0 y) \cos(k_0 z) \\ 0 \end{bmatrix}, \quad (5)$$

where  $k_0$  is the characteristic scale of the external forcing; it is taken as 2 in our study.  $k_0 = 2$  allows the dynamo to develop at large as well as at small length scales.  $F_0$  is the forcing amplitude of the TG forcing. We will study bifurcations in dynamo by varying this parameter. It is best to describe the bifurcations using nondimensional parameters. For the above equation, the two independent nondimensional parameters

are the magnetic Prandtl number ( $P_M$ ), defined as the ratio of  $\nu$  and  $\eta$ , and the magnetic Reynolds number ( $R_m$ ), defined as  $UL/\eta$ , where  $U$  is the characteristic velocity scale and  $L$  is the characteristic length scale of the system. The hydrodynamic Reynolds number ( $Re = UL/\nu$ ) is not an independent parameter and it is related to  $P_M$  and  $R_m$  as  $Re = R_m/P_M$ .

We employ a pseudospectral code, TARANG [21], to numerically solve the above system of equations (Eqs. 1-4) in a cubic box of size  $2\pi$ , with periodic boundary conditions on all sides. TARANG uses Runge-Kutta fourth order scheme for time marching, with  $dt$  dynamically adjusted using the CFL condition ( $dt = \Delta x/\sqrt{20E^u}$ , where  $\Delta x$  is the grid spacing and  $E^u$  is the total kinetic energy). We use the 2/3 rule for dealiasing the simulation runs. We performed more than 150 simulations on  $64^3$  grids. For  $P_M = 1.0$  and 0.5, the dynamo states do not change as we increase the grid resolutions, hence  $64^3$  grid resolution is sufficient for our dynamo simulations. Sometimes, the induced magnetic field vanishes asymptotically after much later time, so we need to perform the above runs for a long time, sometimes ranging up to 10000 eddy turnover times or even higher.

## SIMULATION RESULTS

Numerical simulation for the range of magnetic Prandtl number corresponding to the natural dynamos, e.g., terrestrial liquid sodium experiments ( $P_M \sim 10^{-7}$ ), Earth's interior ( $P_M \sim 10^{-5}$ ), Sun's convective zone ( $P_M \sim 10^{-2}$ ), intergalactic medium ( $P_M \sim 10^{14}$ ), is still an unattainable goal, yet simulations performed at moderate  $P_M$ s ( $\approx 1$ ) provide us insights into some of the fundamental ideas. Also, at moderate  $P_M$  range, we can carry out an extensive study, which is otherwise not possible. We choose  $P_M = 1$  and 0.5 ( $\nu = 0.1$ ,  $\eta = 0.1$  and 0.2) for our study. For all our simulations,  $k_{max}\eta$  (the largest wavenumber times the Kolmogorov length) is always greater than 1.3. Fig. 1 shows a sample of kinetic and magnetic energy spectra for  $P_M = 1$ , which clearly indicates that our simulations are well resolved.

Earlier studies of TG dynamo have typically focused on the studies of total energy, energy spectra, and real space magnetic and velocity fields. In this paper, we will emphasize on the low wavenumber Fourier modes that provide us valuable insights into the dynamo transition. Yadav *et al.* [20] reported, for  $P_M=1$ , that the most dominant velocity Fourier modes are  $(\pm 2, \pm 2, \pm 2)$ ,  $(\pm 4, \pm 4, \pm 4)$ ,  $(\pm 4, \pm 4, 0)$ , and the most dominant magnetic Fourier modes are  $(0, 0, \pm 1)$ ,  $(0, 0, \pm 2)$ ,  $(0, 0, \pm 3)$ ,  $(\pm 2, \pm 2, \mp 3)$ ,  $(\mp 2, \mp 2, \pm 1)$ . The three arguments refer to the  $x$ ,  $y$ , and  $z$  component of the wavenumber. Among the prominent magnetic Fourier modes,  $\mathbf{B}(0, 0, n_z)$  with  $n_z = 1, 2, 3$ , are usually the most energetic ones. Since we are working in a regime with lower Reynolds number, the velocity field maintains the reported 16 TG cell structure for most of the parameter range [20] due to the dominance of the velocity Fourier mode  $\mathbf{u}(2, 2, 2)$ . At much lower Prandtl numbers, the velocity tends to become turbulent, and the TG structures are somewhat washed out.

Fig. 2 illustrates temporal evolution of the dominant magnetic Fourier mode  $\mathbf{B}(0, 0, 1)$ . Barring the no dynamo state (for which all the magnetic Fourier modes are identically zero), typical dynamo states observed in our simulations are portrayed in Fig. 2 and Fig. 3. Figure 2 shows time series of the fixed point (FP), periodic (P), quasiperiodic

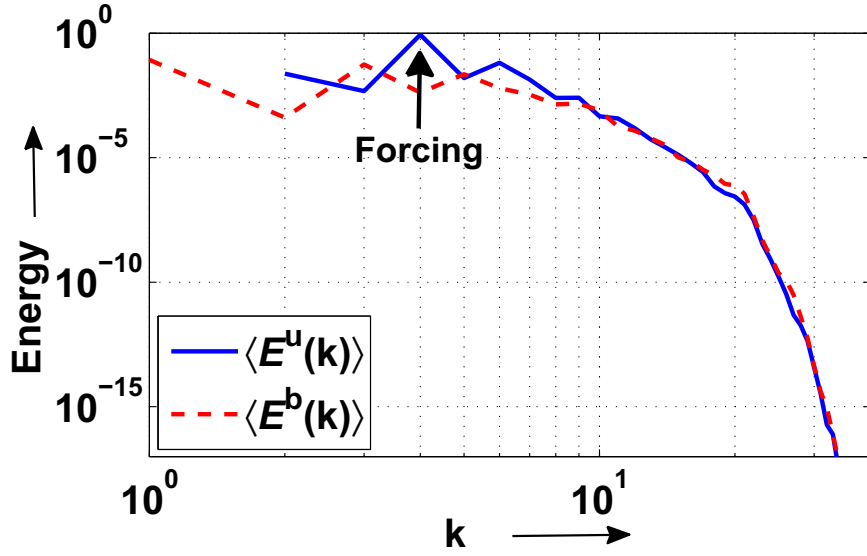


**FIGURE 1.** Time averaged steady state kinetic energy spectrum  $\langle E_u(k) \rangle$  and magnetic energy spectrum  $\langle E_b(k) \rangle$  for  $P_M = 1$  at  $F_0 = 4.8$ . The forced wave-number ( $k_x = k_y = k_z = k_0 = 2$ ) appears as a spike in the energy spectrum. Both the kinetic and the magnetic energy spectrum fall off smoothly to zero indicating that our simulation is well resolved.

(QP), and chaotic states (C). The corresponding phase space projections on  $\mathbf{B}(0,0,1) - \mathbf{B}(0,0,3)$  plane are shown in Fig. 3. FP-state does not show any fluctuations in magnetic field (Fig. 2(a) and Fig. 3(a)) in time. In P-state, the magnetic field oscillates periodically in time (Fig. 2(b) and Fig. 3(b)). In QP-state (Fig. 2(c)), the oscillation of the magnetic field is modulated. The power-spectrum of the time signal shows two incommensurate frequencies. Corresponding filled torus like orbit on the  $\mathbf{B}(0,0,1) - \mathbf{B}(0,0,3)$  plane is shown in Fig. 3(c). The C-state has chaotic temporal fluctuations (Fig. 2(d) and Fig. 3(d)). The power-spectrum of the time signal shows broadband frequencies indicating a chaotic state. Note that many of these temporal behaviors (viz., FP, P, and C-states) of our simulations are qualitatively similar to the dynamo states observed in VKS experiments (see Fig. 2 of [11]).

Time series and phase space plots provide information only for a particular  $F_0$ . Bifurcation analysis, however, is one of the most elegant tools for studying a system for a parameter range. It is not only a concise method for portraying the different states of the system, but it also helps in understanding the different bifurcations of the system. We plot two bifurcations diagrams that bring out some of the interesting features of dynamo transition.

Fig. 4 is a bifurcation diagram for  $P_M = 1$ . Here we exhibit the evolution of the time averaged magnitude of the magnetic mode  $\mathbf{B}(0,0,1)$  as  $F_0$  is varied from 0 to 40 in discrete steps. The inset of the figure provides a closer view just above the dynamo transition. For  $F_0$  below  $\simeq 3.8$ , the dynamo mechanism is not efficient enough to sustain the induced magnetic field; here the induced magnetic field decays asymptotically to zero. For  $F_0 \geq 3.9$ , the system always sustains a magnetic field. Inset of the figure shows the supercritical nature of the dynamo transition [20], which is characterized by

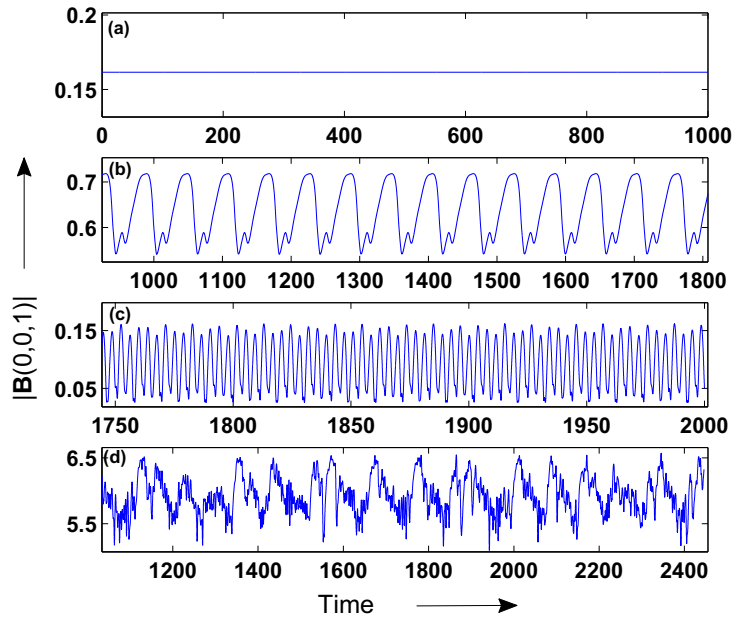


**FIGURE 2.** Time evolution of  $|B(0,0,1)|$  for different values of  $F_0$ : (a) a time-constant state (FP-state) for  $F_0 = 4.1$ ; (b) a time periodic state (P-state) for  $F_0 = 10$ ; (c) a quasiperiodic state (QP-state) for  $F_0 = 36$ ; (d) a chaotic state (C-state) for  $F_0 = 40$ .

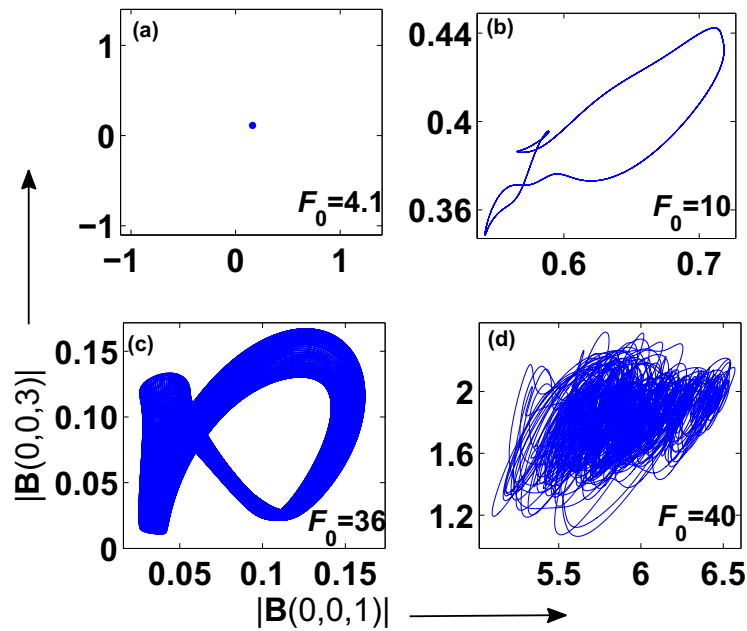


**FIGURE 3.** Phase space projections on the  $(|B(0,0,1)|-|B(0,0,3)|)$  plane for the different states portrayed in Fig. 2. Here the sub-figures (a,b,c,d) correspond to Fig. 2(a,b,c,d) respectively.

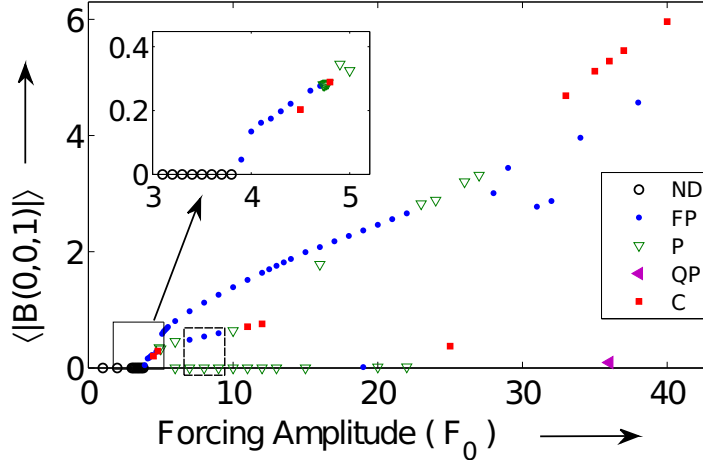


**FIGURE 4.** Bifurcation diagram illustrating the different states observed in our simulation. It depicts the variation of the time averaged magnitude  $\langle |\dots| \rangle$  of the major magnetic Fourier mode  $\mathbf{B}(0,0,1)$  vs.  $F_0$  for  $P_M=1$ . The inset shows the zoomed in view of the boxed region (with solid boundary) of the main figure. Here ND, FP, P, QP, and C stand for no dynamo, fixed point, periodic, quasiperiodic, and chaotic state, respectively. The box with dashed boundary encloses somewhat peculiar coexisting states.

a slow increase in magnetic energy as  $F_0$  is increased ( $E^b \sim \sqrt{R_M - R_M^c}$ ). Notice the existence of two distinct branches: first branch is a trail of blue-colored filled circular-dots, increasing in magnitude as  $F_0$  is increased; second branch is a trail of green-colored hollow triangles on the horizontal axis. We will call the first branch as FP-branch and the other as P-branch. Note that  $\langle |\mathbf{B}(0,0,1)| \rangle \approx 0$  for the P-branch, but the other Fourier mode  $\mathbf{B}(0,0,2)$  is highly active and dominant here, and it maintains the dynamo action (to be described further in the next paragraph). The dashed box in the main figure encloses a set of coexisting states; periodic and fixed-point states having zero and non-zero  $\langle |\mathbf{B}(0,0,1)| \rangle$ , respectively. These co-existing states were obtained by using different sets of initial conditions, and they occur due to the presence of different basins of attraction of dynamical states. There are numerous other coexisting states, some of which have been described in Yadav *et al.* [20].

In another bifurcation diagram, Fig. 5, we plot  $E^b/E^u$  vs.  $F_0$ . The two dominant branches of the figure illustrate important aspects of the dynamo, and they are related to the two branches observed earlier in Fig. 4. The FP-branch gradually settles to a high  $E^b/E^u$  value ( $\simeq 3$ ) and the P-branch settles to a lower  $E^b/E^u$  value ( $< 1$ ). It shows that  $\mathbf{B}(0,0,1)$  plays an important role in the dynamo transition. It is rather interesting to observe that the  $E^b/E^u$  ratio depends quite critically on which low wavenumber modes are dominant. Notice the oval in the figure that encloses the co-existing states (FP-states represented by blue dots, and the P-states represented by inverted green triangles) mentioned in the earlier discussion; these states have approximately equal  $E^b/E^u$ . Another point to note is that the critical magnetic Reynolds number for  $P_M = 1$  is around 19.5 [20].

We also performed numerical simulations for a lower Prandtl number,  $P_M = 0.5$  ( $\nu = 0.1$ ,  $\eta = 0.2$ ). Similar to the case of  $P_M = 1$ , a grid resolution of  $64^3$  was sufficient to

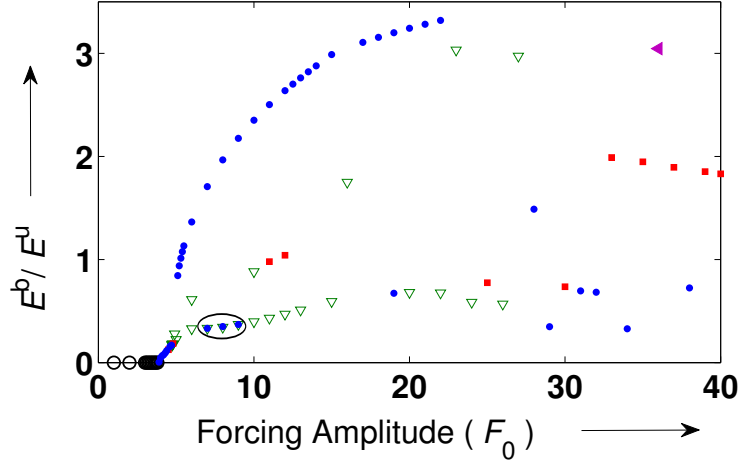


**FIGURE 5.** Bifurcation diagram illustrating the ratio of magnetic and kinetic energy ( $E^b/E^u$ ) vs. the TG forcing amplitude ( $F_0$ ) for  $P_M = 1$ . Presence of distinct branches with  $E^b/E^u$  ranging from small ( $\leq 1$ ) to large values ( $\simeq 3$ ) can be clearly observed in the figure. The oval encloses the states corresponding to the dashed-box in Fig. 4. Refer to Fig. 4 for the description of different points of the figure.

resolve the simulation properly. Similar to  $P_M = 1$  case, we plot bifurcation diagrams for  $\langle |\mathbf{B}(0,0,1)| \rangle$  and  $E^b/E^u$  vs.  $F_0$  as a function of  $F_0$ .

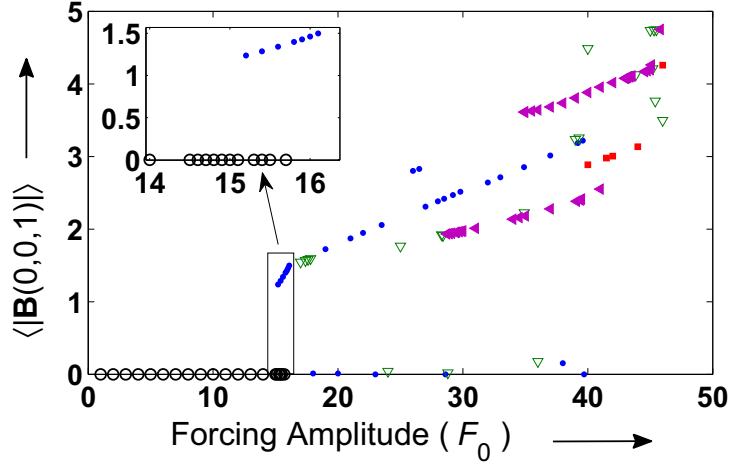
The bifurcation diagrams for  $P_M = 0.5$ , Figs. 6 and 7, have been constructed on the same lines as Figs. 4 and 5, respectively. The first thing which is completely different for  $P_M = 0.5$ , as compared to  $P_M = 1$ , is the nature of dynamo transition. The inset of Fig. 4 near the transition shows a jump in  $\langle |\mathbf{B}(0,0,1)| \rangle$ , as well as a hysteresis, illustrating that the dynamo transition is subcritical.

Fig. 7 illustrates that the  $E^b/E^u$  ratio for  $P_M = 0.5$  is very different from that for  $P_M = 1$ . Except for some points, throughout the explored range of  $F_0$  for  $P_M = 0.5$ , the system has  $E^b/E^u$  less than or equal to one. There are many other interesting features for  $P_M = 0.5$  dynamo. For example, the route to chaos for one of the chaotic windows is via a quasiperiodic route. We are investigating these features and they will be presented in future.

## CONCLUSION

In this paper, we show that Taylor-Green dynamo shows a rich behavior near dynamo transition. The nature of dynamo transition depends quite critically on the magnetic Prandtl number. It shows supercritical and subcritical bifurcations for  $P_M = 1$  and 0.5 respectively. Also, near the transition, the system is governed by a small number of large-scale or low wavenumber Fourier modes. For  $P_M = 1$ , the system can have low as well as high  $E^b/E^u$  (0 to 3) depending on which of the magnetic Fourier mode is active. For  $P_M = 0.5$ , the ratio  $E^b/E^u$  is less than equal to one.

In our simulations, we observe various dynamo states, such as constant, time-periodic, quasiperiodic, and chaotic magnetic fields. In some sense, they replicate the various



**FIGURE 6.** Bifurcation diagram illustrating time averaged magnitude of the major magnetic Fourier mode  $\mathbf{B}(0,0,1)$  vs.  $F_0$  for  $P_M = 0.5$ . The inset shows the zoomed in view of the boxed region of the main figure. Refer to Fig. 4 for the description of different points of the figure.

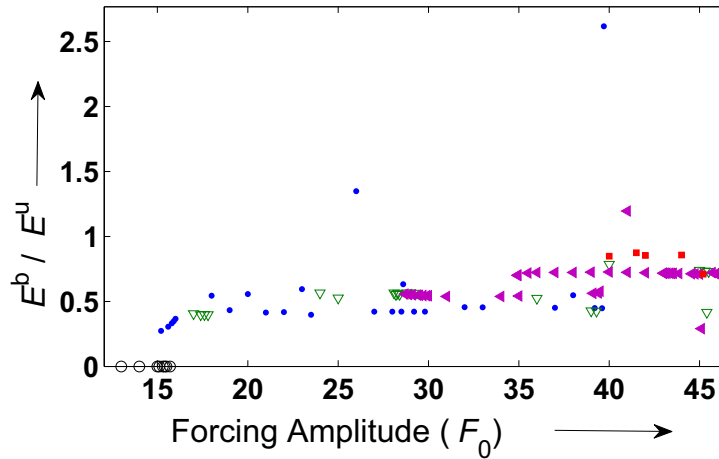


**FIGURE 7.** Bifurcation diagram: ratio of magnetic and kinetic energy ( $E^b/E^u$ ) vs.  $F_0$  for  $P_M = 0.5$ .

dynamo states observed in VKS experiment [11]. We also observe multiple coexisting dynamo states for a given  $P_M$  and  $F_0$  by varying the initial conditions. These features have been described in detail in Yadav *et al.* [20].

We are in the process of investigating the dynamo features for much lower and much higher Prandtl numbers ( $\approx 0.1, 0.01, 10, 100$ ). These simulations require much higher resolution, and extensive analysis is very demanding. We hope to be able to relate these simulations to realistic laboratory experiments, geodynamo, and solar dynamo. These results will be reported in future.

## ACKNOWLEDGMENTS

We thank Stephan Fauve for fruitful discussions and comments. This work was supported by a research grant of DST India as Swarnajayanti fellowship to MKV. We thank the HPC committee of IIT Madras for granting us computational time on VEGA cluster on which some of the numerical simulations were performed.

## REFERENCES

1. J. Larmor, *Rep. Brit. Assoc. Adv. Sci.* **87**, 159 (1919).
2. H. K. Moffatt, *Magnetic Field Generation in Electrically Conducting Fluids*, Cambridge University Press, Cambridge, U.K., 1978.
3. F. Krause, and K. H. Radler, *Mean-field Magnetohydrodynamics and Dynamo Theory*, Pergamon press, Oxford, U.K., 1980.
4. A. Brandenburg and K. Subramanian, *Phys. Rep.* **417**, 1–209 (2005).
5. A. Gailitis et al., *Phys. Rev. Lett.* **84**, 4365–4368 (2000).
6. A. Gailitis et al., *Phys. Rev. Lett.* **86**, 3024–3027 (2001).
7. R. Stieglitz and U. Müller, *Phys. Fluids* **13**, 561–564 (2001).
8. R. Monchaux et al., *Phys. Rev. Lett.* **98**, 044502 (2007).
9. M. Berhanu et al., *Europhys. Lett.* **77**, 59001 (2007).
10. S. Aumaître et al., *Comptes Rendus Physique* **9**, 689–701 (2008).
11. F. Ravelet et al., *Phys. Rev. Lett.* **101**, 074502 (2008).
12. F. Pétrélis, N. Mordant, and S. Fauve, *Geophys. Astrophys. Fluid Dyn.* **101**, 289–323 (2007).
13. Y. Ponty, P. D. Mininni, D. C. Montgomery, J.-F. Pinton, H. Politano, and A. Pouquet, *Phys. Rev. Lett.* **94**, 164502 (2005).
14. Y. Ponty, P. D. Mininni, J.-F. Pinton, H. Politano, and A. Pouquet, *New J. Phys.* **9**, 296 (2007).
15. A. B. Iskakov, A. A. Schekochihin, C. S. Cowley, J. C. McWilliams, and M. R. E. Proctor, *Phys. Rev. Lett.* **98**, 208501 (2007).
16. P. D. Mininni, Y. Ponty, D. C. Montgomery, J.-F. Pinton, H. Politano, and A. Pouquet, *ApJ* **626**, 853–863 (2005).
17. C. Nore, M. E. Brachet, H. Politano, and A. Pouquet, *Phys. Plasmas* **4**, 1–3 (1997).
18. M. K. Verma, T. Lessinnes, D. Carati, I. Sarris, K. Kumar, and M. Singh, *Phys. Rev. E* **78**, 036409 (2008).
19. R. Donner, N. Seehafer, M. A. F. Sanjuán, and F. Feudel, *Physica D* **223**, 151–162 (2006).
20. R. Yadav, M. Chandra, M. K. Verma, S. Paul, and P. Wahi, *Europhys. Lett.* **91**, 69001 (2010).
21. TARANG: An object oriented code for turbulence simulations. *Unpublished*.